In situ continuous decoding of temperature humidity and micro strain during sandstone fracture hole restoration

Check for updates

Ruoxu Zhao, Yang Liu, Quanhua Xie, Yuanyuan He & Nianbing Zhong ✉

To investigate sodium silicate slurry curing mechanisms and sandstone interactions during crack restoration, an in-situ fiber Bragg grating (FBG) sensor system was established to monitor temperature, humidity, and micro-strain during curing. The surface morphology and material composition of sodium silicate slurry at different temperatures were also investigated. The results indicated that CH_3COOH from $CH_3COOCH_2CH_2OOCCH_3$ hydrolysis reacted with $Na_2O \cdot nSiO_2$, generating heat (max heating rate: 0.42 °C/h at 35 °C), reducing humidity (max dehumidification rate: 0.79% RH/h at 35 °C), and inducing shrinkage strain (peak at −115.23 με at 35 °C). The grout achieved optimal curing, forming a densified structure with small CH_3COONa migration, inducing only 31.62 με micro-strain on the sandstone surface at 35 °C. Smaller fissures reduced sandstone strain and damage, confirming sodium silicate is more suitable for small fissures at 35 °C. This study advances heritage conservation and fiber optic sensing via intelligent relic preservation technologies.

As a common type of rock, sandstone is widely distributed globally and serves as the primary material for many cultural heritage sites such as ancient buildings, sculptures, and grottoes[1]. It not only possesses immense historical and artistic value but also represents a precious legacy of human civilization. However, due to long-term exposure to natural environments and anthropogenic factors, These artifacts are often susceptible to water damage, weathering, and microbial deterioration, which subsequently lead to the formation of cracks, necessitating effective restoration and conservation measures. Therefore, the effective restoration of cracks in sandstone is crucial for extending their lifespan[2].

Currently, the primary crack restoration methods in sandstone include support reinforcement[3], bolt-anchor reinforcement[4], and grouting restoration[5–10]. While support reinforcement can enhance the load-bearing capacity of cultural relics to a certain extent, it may also impact their appearance and overall integrity[3]. bolt-anchor reinforcement can enhance the internal connectivity strength, but may result in surface damage to the cultural relic and increase the risk of secondary damage[4]. Among these, grouting restoration is the most common and effective method, allowing for the selection of suitable grouting materials based on crack size. It can fill significant fault zones and superficial cracks caused by geological movement, physicochemical weathering, microbial erosion, and other damaging factors. Grouting materials include natural hydraulic lime[5], acrylic resins[6], metakaolin[7], and sodium silicate slurry[8–10]. Sodium silicate grout slurry is one of the most widely used chemical grouting materials owing to its low cost, adjustable setting time, high strength, and low viscosity[8]. It demonstrates superior physical and chemical stability, as well as enhanced permeability and adhesion during the curing process. Zullo[9] prepared sodium silicate-based grouting materials and injected them into boreholes at the Camaldoli site, verifying the effectiveness of the sodium silicate-based grouting materials. Fang[10] utilized sodium silicate-doped cement-based grouting materials for the grouting restoration of cracks in the cliff body of Klippe in Hangzhou. The results indicated that the incorporation of sodium silicate could enhance the durability of the hardened grout and improve the restoration effectiveness. These results highlight the potential of sodium silicate slurry in various restoration applications.

Temperature, humidity, and micro-strain during the sodium silicate grout curing process are crucial factors that affect both the grouting effect and the sandstone itself. Excessively high or low temperatures can lead to incomplete curing and reduced the slurry strength[11]. Changes in humidity can affect the hygroscopicity and expansibility of the grouting material,

Chongqing Key Laboratory of Optical Fiber Sensor and Photoelectric Detection, Chongqing Key Laboratory of Modern Photoelectric Detection Technology and Instruments, Chongqing Engineering Research Center of Intelligent Optical Fiber Sensing Technology, Chongqing University of Technology, Chongqing, China. ✉e-mail: zhongnianbing@163.com

further affecting its bonding strength and durability with the sandstone rock mass[11,12]. Micro-strain variations in the grouting material directly affect its bonding state with the sandstone rock mass[13]. Additionally, the micro-strain on the rock mass surface is one of the most crucial indicators that directly represents the damage intensity to the cultural relic during the crack restoration process of the rock mass[14,15]. Therefore, in situ and continuous decoding of temperature, humidity, and micro-strain of the sandstone and grout are key to revealing the solidification mechanism of the slurry and the interaction between the slurry and sandstone during the crack repair process.

The decoding techniques for grouting materials and the physical properties of sandstone primarily include scanning electron microscopy (SEM)[16,17], Fourier-transform infrared spectroscopy (FTIR)[18,19], and nuclear magnetic resonance (NMR)[8,11]. Infrared thermal imaging (IRT)[20] has also been used. While these techniques can provide important information regarding pore structure, chemical composition, diffusion characteristics, and distribution, they face challenges in terms of achieving real-time in situ monitoring. This includes the temperature, humidity, and micro-strain during the grouting material curing process and the resulting micro-strain changes in the fractured structures. Fiber Bragg grating (FBG) sensors exhibit high sensitivity, strong anti-interference capabilities, and compact size. They can also perform quasi-distributed measurements and have been widely applied to temperature, humidity, and micro-strain detection[21]. For example, Giovanna Palumbo conducted an experimental evaluation utilizing FBGs for real-time temperature and early-stage shrinkage monitoring of geopolymer matrices[22]. Jun-Yi Guo Developed an FBG-based humidity sensor suitable for unsaturated soils, conducted measurements and analyses of humidity in various sand-kaolin mixtures, and verified the feasibility of the sensor in unsaturated soils[23]. However, there have been no reports on the application of FBG sensors for real-time in situ temperature, humidity, and micro-strain monitoring during the grouting material curing process or for micro-strain on the sandstone surface.

To obtain in situ online data on the temperature, humidity, and micro-strain spatial distribution within the grout and the micro-strain on the sandstone surface, sandstone samples with varying hole diameters were designed and prepared. These samples were created to simulate the sandstone deterioration characteristics. A mathematical model for temperature, humidity, and micro-strain detection using FBG sensors was established. FBG sensors for temperature, humidity, and micro-strain were developed, and a detection system was constructed. An FBG detection system was used to acquire real-time data on the curing process, including the temperature, humidity, and micro-strain in sandstone holes and the micro-strain on the surface. Optical microscopy, field-emission SEM (FESEM), X-ray photoelectron spectroscopy (XPS), and X-ray diffraction (XRD) were employed to characterize the morphology and composition of the sandstone samples before and after restoration. The results revealed the relationships between the internal temperature, humidity, shrinkage strain, and micro-strain on sandstone surfaces during the grouting process. The grout diffusion, transport characteristics and its curing reaction products within the sandstone were also analyzed. The findings of this study enhance our understanding of the curing mechanisms of chemical grouts in repairing sandstone cracks and the interaction mechanisms between grouting materials and sandstone bodies. Additionally, they help evaluate the effectiveness and reliability of grout in repairing sandstone fissures and aid in accurately assessing the damage caused to cultural relics during curing.

Methods
Experimental materials
The Polyvinyl alcohol (degree of alcoholysis: 98.0–99.0 mol%), chitosan (degree of deacetylation: ≥ 95%), glacial acetic acid (purity: 99.8%), concentrated sulfuric acid, ethylene glycol diacetate (≥ 99%), and silane coupling agent used in this study were all analytical grade. Analytical grade materials were purchased from Aladdin Biochemical Technology Co., Ltd.

(Shanghai, China). The sodium silicate solution (Baume degree: 40 Bé; modulus: 3.1 ~ 3.4) was purchased from Tianjin Huashi Chemical Reagent Co., Ltd. The epoxy resin was obtained from Huibo New Materials Technology Co., Ltd. The stainless steel capillary had inner and outer diameters of 450 and 600 μm, respectively, and a length of 2 cm. The porous stainless steel tube had inner and outer diameters of 3 and 4 mm, respectively, and a length of 3 cm. FBG was purchased from Beijing Tongwei Technology Co., Ltd., with an optical fiber cladding diameter of 125 μm, core diameter of 10 μm, and a grating region length of 10 mm.

Sandstone sample preparation
The sandstone cylindrical sample, simulating stone cultural relics, had a diameter and length of 5 and 10 cm, respectively, and was purchased from Shandong Yuze Stone Industry Co., Ltd. To simulate damaged stone cultural relics, a hole was drilled at the center of the top of the sandstone sample, with a depth of 8 cm and diameters of 1, 2 and 3 cm for the grouting restoration experiments and sensor installation for in situ real-time monitoring. Before conducting the grouting experiments, the sandstone sample was placed in a drying oven at 80 °C for 24 h for preparation.

Slurry preparation
Subsequently, 20 ml of sodium silicate solution was added to 10 ml of deionized water and 3.8 ml of diethylene glycol diacetate solution. The resulting solution was stirred for 5 min to obtain the grouting sodium silicate material for sandstone pore restoration, as shown in Fig. S6.

Slurry curing mechanism
When sandstone cracks are restored with sodium silicate slurry, diethylene glycol diacetate ($CH_3COOCH_2CH_2OOCCH_3$) undergoes hydrolysis, producing acetic acid (CH_3COOH)[24]:

$$CH_3COOCH_2CH_2OOCCH_3 + H_2O \rightleftharpoons HOCH_2CH_2OH + 2CH_3COOH \tag{1}$$
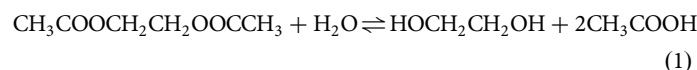
Subsequently, the main slurry component, sodium silicate ($Na_2O \cdot nSiO_2$), reacts with the hydrolysis product, acetic acid (CH_3COOH), to produce sodium acetate (CH_3COONa), silica (SiO_2), and water (H_2O)[24]:

$$Na_2O \cdot nSiO_2 + 2CH_3COOH \rightarrow 2CH_3COONa + nSiO_2 \downarrow + H_2O \tag{2}$$
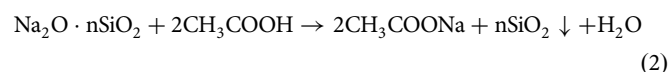
where n is the sodium silicate modulus, which indicates the SiO_2 to Na_2O molar ratio. The CH_3COONa generated in reaction is dehydrated to form $C_2H_3NaO_2 \cdot 3H_2O$[25]. $Na_2O \cdot nSiO_2$ readily reacts with CO_2 in air[26]:

$$Na_2O \cdot nSiO_2 + CO_2 \rightarrow Na_2CO_3 + nSiO_2 \downarrow \tag{3}$$
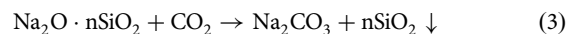
After the sodium silicate slurry curing reaction with diethylene glycol diacetate is completed, the resulting CH_3COONa and SiO_2 mixture serves as a solid material for sandstone crack restoration. This solid material offers several advantages, including good compatibility with sandstone, high strength, corrosion resistance, excellent thermal stability, and non-toxicity[26,27].

Sensor preparation and packaging
FBG Humidity Sensor (FBG-H). To enable the FBG sensor to detect humidity, a polyvinyl alcohol (PVA)–chitosan humidity-sensitive hydrogel was prepared. One gram of chitosan powder was added to 20 ml of 4% glacial acetic acid solution and stirred at room temperature for 4 h. Then, 1.5 g of PVA powder was dissolved in 12 ml of deionized water and stirred in a 95 °C water bath for 3 h. Finally, 2 ml of the PVA solution was added to the prepared chitosan solution and stirred at room temperature for 6 h to obtain the PVA-chitosan hydrogel (Fig. S3). Next, the FBG was pre-treated as follows: (i) The FBG was immersed in 98%

concentrated sulfuric acid for 60 min to remove the polyacrylate coating. Then, the fiber grating region was cleaned with anhydrous ethanol and deionized water for 10 min and left to dry at room temperature. (ii) The fiber grating was placed in a 10% silane coupling agent for 30 min to enhance the adhesion strength of the humidity-sensitive film on the fiber surface. After removal, it was rinsed with deionized water and placed in a vacuum drying oven at 90 °C for 15 min. (iii) Finally, a humidity-sensitive material was coated and the lift-off method was used to apply the humidity-sensitive material to the FBG surface. A pair of tweezers was used to pick up 0.1 g of hydrogel, controlling the tweezers to slowly lift along the fiber grating, and then placed in a drying oven at 60 °C for 20 min. This operation was repeated five times, resulting in a humidity-sensitive film with a thickness of 59 μm formed around the fiber grating region (Fig. S4). The FBG-H response characteristics to humidity, temperature, and micro-strain are shown in Figs. S1–2.

FBG Micro-Strain Sensor (FBG-S). To monitor strain changes during the slurry curing process and eliminate strain interference from the humidity detection results, an untreated bare FBG was introduced as a micro-strain sensor (Fig. 1). The sensor was in direct contact with the slurry or sandstone surface. An FBG strain sensor in contact with the slurry was used to detect the temperature and micro-strain changes during the slurry curing process. The FBG-S response characteristics to micro-strain and temperature are shown in Figs. S1–2.

FBG Temperature Sensor (FBG-T). To accurately monitor the temperature changes during the slurry curing process, a stainless-steel capillary tube was utilized. The tube had an inner diameter of 450 μm and a length of 20 mm. It was used to package the bare FBG and eliminate temperature interference from the micro-strain and humidity measurement results. The ends were sealed with epoxy resin to prevent the slurry from entering the tube during testing. The sealed sensor served as a temperature sensor (Fig. 1 and S4a), ensuring that the measurement process was unaffected by slurry strain. The FBG-T response characteristics to temperature are shown in Fig. S2.

Integrated FBG-T, FBG-H, and FBG-S packaging. To simultaneously measure the temperature, humidity, and micro-strain at the same location while providing effective sensor protection, a porous stainless-steel tube (PSST) was employed. This tube had an inner diameter of 3 mm and length of 25 mm, encasing the grating areas of the FBG temperature, humidity, and strain sensors. The end of the FBG was fixed using epoxy resin (Fig. 1 and S4b).

Temperature and humidity detection and micro-strain measurement principle

As the external temperature changes, the FBG effective refractive index also changes. Simultaneously, thermal expansion causes the grating period to

Fig. 1 | Schematic of the sensor and measurement system structure.

change, leading to a drift in the FBG center wavelength (λ_B) owing to temperature variations. The total FBG wavelength shift ($\Delta\lambda_{B\_1}$) under the influence of temperature alone is given by[28]:

$$\Delta\lambda_{B\_1} = \lambda_{B\_1}\Delta T(\alpha + \varsigma) = K_{T\_1}\Delta T \tag{4}$$

Where a is the thermal expansion coefficient of the optical fiber material, ς is the thermo-optic coefficient, ΔT is the temperature change, and K_{T_1} is the temperature sensitivity coefficient. However, because of the photo-elastic effect in optical fibers, strain can cause a drift in λ_B. Therefore, when an optical fiber is affected by external strain, it is sensitive to both strain and temperature. The drift of the Bragg center wavelength ($\Delta\lambda_{B\_2}$) is defined as follows[29]:

$$\Delta\lambda_{B\_2} = \lambda_{B\_2}[(1 - P_\varepsilon)\Delta\varepsilon + (\alpha + \varsigma)\Delta T] = K_{\varepsilon\_1}\Delta\varepsilon + K_{T\_2}\Delta T \tag{5}$$

Where P_ε is the optical fiber optical elasticity coefficient, $\Delta\varepsilon$ is the strain variation experienced by the optical fiber, and K_{ε_1} and K_{T_2} are the strain and temperature sensitivity coefficients, respectively.

When a humidity-sensitive material is coated onto the FBG surface, the material undergoes hygroscopic expansion and desorption-induced contraction. The resulting tensile or compressive axial strain is transmitted to the fiber grating, leading to a shift in the Bragg resonance center wavelength[28]. Therefore, the Bragg center wavelength ($\Delta\lambda_{B\_3}$) of the humidity sensor can be defined as:

$$\Delta\lambda_{B\_3} = \lambda_{B\_3}[(1 - P_e)\varepsilon_{RH} + (1 - P_e)\varepsilon_T + (1 - P_e)\Delta\varepsilon + \varsigma\Delta T] \tag{6}$$

Where ε_{RH} denotes the humidity expansion coefficient, ε_T represents the fiber thermal expansion coefficient after coating with a humidity-sensitive film, and $\Delta\varepsilon$ is the strain variation experienced by the fiber grating itself. The former are expressed as:

$$\varepsilon_{RH} = [\frac{A_M E_M}{A_M E_M + A_f E_f}](\alpha_{M(RH)} - \alpha_{f(RH)})\Delta RH \tag{7}$$

$$\varepsilon_T = [\frac{A_M E_M}{A_M E_M + A_f E_f}](\alpha_{M(T)} - \alpha_{f(T)})\Delta T \tag{8}$$

Where A_M and A_f represent the cross-sectional areas of the humidity-sensitive film and optical fiber, respectively; E_M and E_f denote the Young's moduli of the humidity-sensitive film and optical fiber, respectively; $a_{M(RH)}$ and $a_{M(T)}$ represent the humidity and thermal expansion coefficients of the humidity-sensitive film, respectively; and $a_{f(RH)}$ and $a_{f(T)}$ represent the humidity and thermal expansion coefficients of the optical fiber, respectively. Because the bare FBG was insensitive to humidity, the humidity expansion coefficient was 0. From (6), it can be concluded that:

$$\Delta\lambda_{B\_3} = \lambda_{B\_3}(K_{RH}\Delta RH + K_{\varepsilon\_2}\Delta\varepsilon + K_{T\_3}\Delta T) \tag{9}$$

Where ΔRH represents the humidity change and K_{RH}, K_{ε_2}, and K_{T_3} denote the humidity, strain, and temperature sensitivities, respectively. Here, K_{RH} can be expressed as:

$$K_{RH} = (1 - P_e)[1 - \frac{E_f r_f^2 C_0}{E_f r_f^2 + E_M(t^2 + 2tr_f)}]\alpha_{M(RH)} \tag{10}$$

Where r_f represents the optical fiber radius; t is the humidity-sensitive film thickness; and C_0 is the surface bonding coefficient between the fiber grating and the humidity-sensitive film. At this point, the humidity sensor is simultaneously influenced by the temperature, strain, and humidity. To eliminate the effects of temperature and strain, temperature and strain sensors were used as the temperature and strain compensation units of the humidity sensor, respectively. Based on Eqs.(4), (5), (6) and(10), a matrix
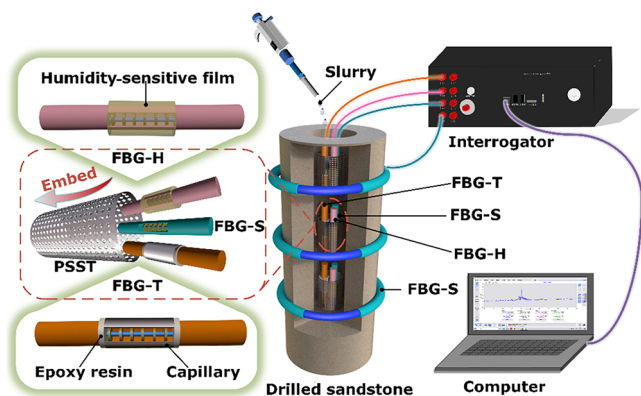
model can be established as follows[29]:

$$\begin{bmatrix} \Delta\lambda_{B\_1} \\ \Delta\lambda_{B\_2} \\ \Delta\lambda_{B\_3} \end{bmatrix} = \begin{bmatrix} K_{T\_1} & 0 & 0 \\ K_{T\_2} & K_{\varepsilon\_1} & 0 \\ K_{T\_3} & K_{\varepsilon\_2} & K_{RH} \end{bmatrix} \begin{bmatrix} \Delta T \\ \Delta\varepsilon \\ \Delta RH \end{bmatrix} \qquad (11)$$

Through calibration experiments (Figs. S1–2), the humidity sensitivity coefficient of the humidity sensor (K_{RH}) was found to be 11.3 pm/%RH. The strain sensitivity coefficient (K_{ε_2}) was 1.3 pm/με, and the temperature sensitivity coefficient (K_{T_3}) was 13.4 pm/°C. The strain sensitivity coefficient of the micro-strain sensor (K_{ε_1}) was 1.3 pm/με, and the temperature sensitivity coefficient (K_{T_2}) was 9.9 pm/°C. The temperature sensitivity coefficient of the temperature sensor (K_{T_1}) was 9.9 pm/°C. By substituting the sensitivity coefficients of the above sensors into (11), the matrix model is obtained as follows:

$$\begin{bmatrix} \Delta\lambda_{B\_1} \\ \Delta\lambda_{B\_2} \\ \Delta\lambda_{B\_3} \end{bmatrix} = \begin{bmatrix} 9.9 & 0 & 0 \\ 9.9 & 1.3 & 0 \\ 13.4 & 1.3 & 11.3 \end{bmatrix} \begin{bmatrix} \Delta T \\ \Delta\varepsilon \\ \Delta RH \end{bmatrix} \qquad (12)$$

Therefore, by using the FBG demodulator, the drift of the Bragg center wavelength from the temperature, humidity, and micro-strain sensors can be collected in real time. Combining these data with Eq.(12) allows obtaining accurate information on temperature, humidity, and micro-strain during the sodium silicate curing process in rock fractures, as well as micro-strain changes on the rock surface.

Monitoring system for sandstone pore grouting repair process parameters

The temperature, humidity, and micro-strain monitoring system used for the sandstone pore-grouting repair process is shown in Fig. 1 and S7. This detection system mainly consisted of a fiber sensor array, FBG demodulator, sandstone sample, sodium silicate slurry, and a temperature and humidity control chamber. The fiber sensor array included three sets of integrated FBG sensors for the in situ detection of the temperature, humidity, and micro-strain distribution within the sandstone cracks. Additionally, it comprises three sets of FBG-S to detect the micro-strain distribution on the sandstone surface. The FBG demodulator (SM125-500, Micron Optics Inc.) had a light source bandwidth of 1510–1590 nm, wavelength resolution of 1 pm, and a sampling interval of 0.5 s. The three sets of temperature, humidity, and micro-strain sensing units within the sandstone cracks were positioned at heights of 2, 5, and 8 cm, respectively. The strain sensors on the sandstone surface were wrapped around the sandstone sample at the same height and secured with epoxy resin. The prepared sodium silicate slurry was uniformly injected into the holes using a syringe, and curing was performed under controlled temperature and humidity conditions.

Analytical methods

The surface morphology of the samples was characterized using a camera (D5200, Nikon, Japan), an optical microscope (BK6000, OTT Optics), and FESEM (Zeiss Sigma HD). The setup was equipped with an energy-dispersive X-ray spectroscopy (EDS) system for elemental analysis. The sample composition was investigated via XRD and XPS. For XRD analysis (using a Japan RIGAKU Smartlab X-ray diffractometer), Cu radiation was employed at a tube voltage of 40 kV and current of 100 mA, with a scanning speed of 2 °/min. For XPS analysis (using a Thermo Fisher Nexsa photoelectron spectrometer), Mo target Kα radiation was used, with the sample binding energy referenced to the carbon peak C1s (284.8 eV).

Results

To investigate the morphological characteristics of the sandstone matrix and slurry after curing at different temperatures, the slurry (25.12 ml) was injected into the cracks in the sandstone sample (diameter: 2 cm). Then, the

samples were cured in −5, 15, 35, 55, and 75 °C environments for 7 d, with a relative humidity (RH) of 20%, 50%, 40%, 15%, and 5%, respectively. The morphological features of the samples were observed using a camera, optical microscopy, and FESEM, as shown in Fig. 2.

As shown in Fig. 2a–e, the sandstone surface morphology exhibits significant differences after sodium silicate slurry curing at different temperatures. After curing at 55 and 75 °C, the sandstone surface morphology did not change significantly. At -5 °C, the surface of the sandstone sample showed signs of water spots. After curing at 35 °C, a small amount of crystallization appeared on the surface of the sandstone sample. The most noticeable changes occurred after curing at 15 °C, where a large amount of white crystalline salt was precipitated. As can be seen in Fig. 2f–j, the overall slurry volume exhibits minimal reduction after curing at −5 and 75 °C. By contrast, the slurry shrank to varying degrees after curing at 15, 35, and 55 °C.

As shown in Fig. 2k–o, the sandstone cross-sectional body color is light yellow, which is attributed to the sandstone being yellow sandstone, primarily composed of quartz, kaolinite, and srebrodolskite[30,31]. After curing the slurry in the sandstone cracks at −5, 55, and 75 °C, the sandstone retained its light yellow color. However, after curing at 15 and 35 °C, white salts appeared in the cross-section of the sandstone sample. These white crystalline salts precipitated from the inside, creating a distinct boundary between the yellow crystals and white crystalline salts, as shown in Fig. 2l, m.

As shown in Fig. 2p, significant unreacted material accumulated on the surface of the product cured at −5 °C. This is attributed to the slow reaction rate of the slurry in the sandstone holes at −5 °C. Figure 2q–s show varying degrees of white crystal accumulation on the surface morphology of the cured products within a temperature range of 15–55 °C, with the white crystals being most uniformly distributed and densely structured at 35 °C (Fig. 2r). This uniformity is due to the more complete reaction between sodium silicate ($Na_2O·nSiO_2$) in the slurry and the hydrolysis product, ethylene glycol diacetate ($CH_3COOCH_2CH_2OOCCH_3$)[8]. By contrast, the slurry cured at 75 °C exhibits noticeable cracks (Fig. 2t), caused by internal strain generated from the excessively high temperature, which leads to structural damage of the slurry.

As shown in Fig. 2u, the surface structure of the product cured at −5 °C consists of larger aggregate structures. This is because of the slow reaction of the slurry at such low temperatures, which led to significant unreacted material aggregation. Figure 2v indicates that the surface of the product cured at 15 °C has numerous small-sized particles, resulting in a rough and porous surface morphology with improved material density. Figure 2w reveals a smooth and dense surface of the product cured at 35 °C, with good dispersion, further confirming that the slurry reacted most thoroughly at this temperature. Figure 2x and S9 show numerous acicular crystals on the surface of the product cured at 55 °C, which is attributed to rapid nucleation when the Si concentration reached the supersaturation threshold during the slurry dehydration and condensation processes[26]. Additionally, cracks begin to form on the surface of the cured product because of internal thermal expansion during the curing process[32,33]. As shown in Fig. 2Y, the surface of the product cured at 75 °C exhibits numerous cracks. These cracks result from excessively rapid temperature increases during the curing process, which cause excessive internal thermal expansion stress, ultimately leading to severe damage to the internal structure.

As shown in Fig. 2, when the slurry is cured at 35 °C, it permeates from the inside of the sandstone to the outside, forming crystalline salts both within the sandstone and on its surface. To determine the sandstone compositional and microstructural changes before and after slurry curing, XRD, XPS, and EDS were used to characterize the sandstone samples, as shown in Fig. 3 and S8.

As shown in Fig. 3a, the main component of the sandstone sample before grouting is quartz, along with trace amounts of kaolinite and srebrodolskite[30,31]. After grouting, a significant $C_2H_3NaO_2·3H_2O$ characteristic peak was observed in the sandstone sample. This is attributed to the reaction between the sodium silicate($Na_2O·nSiO_2$) and the acetic acid (CH_3COOH) produced from the ethylene glycol diacetate ($C_6H_{10}O_4$)
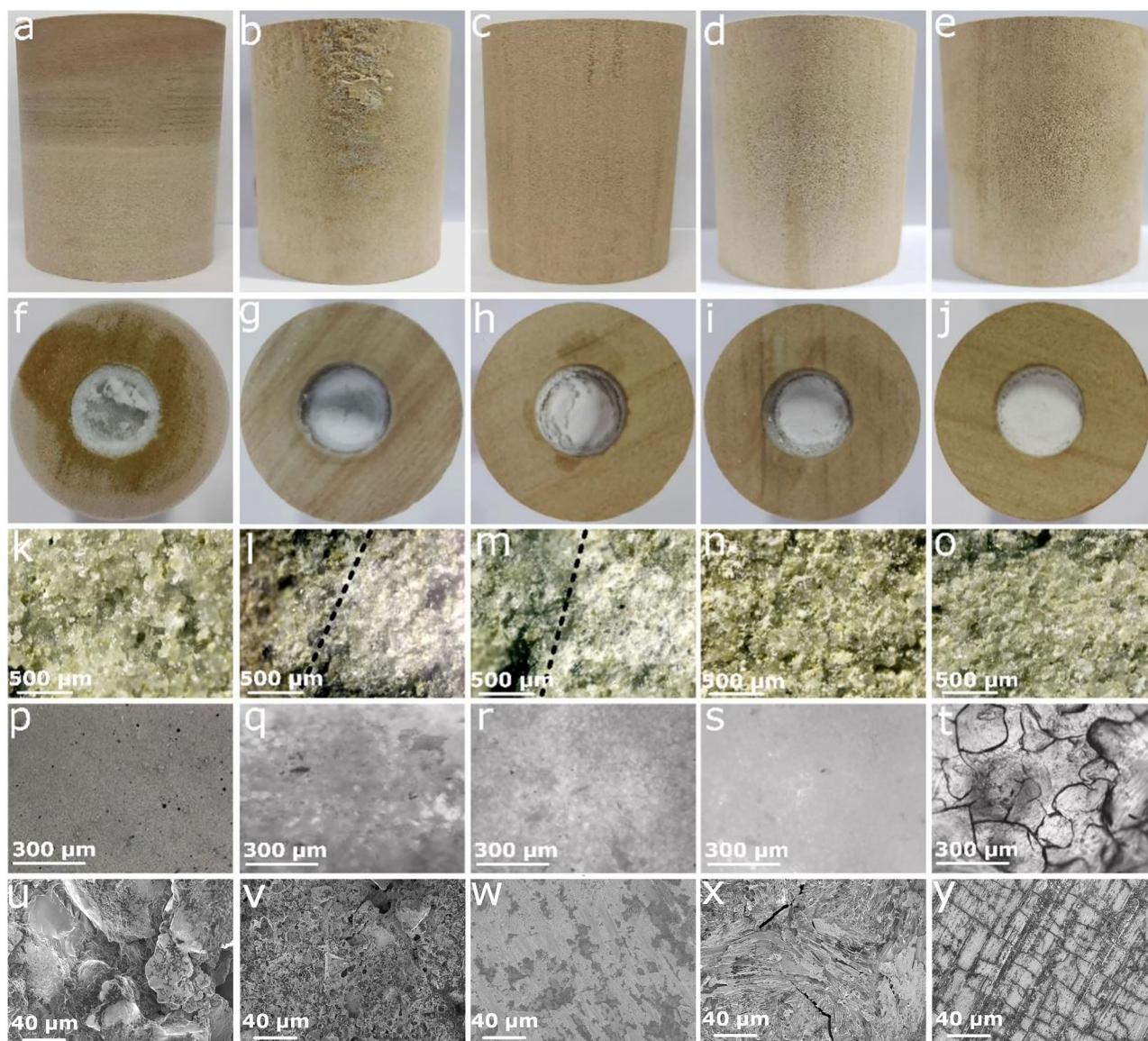
Fig. 2 | Morphology images of the sandstone and slurry. a–e Side images of the sandstone samples after water glass slurry curing at -5, 15, 35, 55, and 75 °C, respectively. **f–j** Top images of the sandstone samples under the same curing conditions. **k–o** Optical microscopy images of sandstone cross-sections cured at −5, 15, 35, 55, and 75 °C, respectively. **p–t** Surface optical microscopy images of curing products inside the cracks at −5, 15, 35, 55, and 75 °C. **u–y** Surface FESEM images of curing products inside the cracks at −5, 15, 35, 55, and 75 °C.

hydrolysis, as described in Reaction (2). This reaction forms sodium acetate (CH$_3$COONa) and silica (SiO$_2$) with water evaporation from sodium acetate, resulting in the formation of white crystalline C$_2$H$_3$NaO$_2$·3H$_2$O. Figure 3b shows that the post-grouting sandstone sample mainly contains six elements: Mg, Na, O, Ca, C, and Si. The significant increase in the sodium and carbon contents after grouting suggests the formation of sodium organic salts. Figure 3c shows that the binding energy of Si 2p in the pre-grouting sample is located at 102.88 eV, indicating that Si predominantly exists as SiO$_2$ in sandstone[34]. This finding is further corroborated by the XRD data presented in Fig. 3a, which confirm that quartz is the main crystal phase in the sandstone. Figure 3d displays C 1 s peaks at 284.8, 286.88, and 288.51 eV, corresponding to C-C, C-O, and C = O bonds[35,36], respectively, suggesting that carbon primarily exists in the form of CH3COO⁻. Figure 3e shows O 1 s peaks at 531.78 and 536.40 eV, which correspond to C-O and C = O bonds[37], respectively. Meanwhile, Fig. 3f indicates that the Na 1 s peak is primarily located at 1070.9 eV, further confirming that the main product on the surface of the post-grouting sample is C$_2$H$_3$NaO$_2$·3H$_2$O. Additionally, Fig. S8 shows an increase in the O and Si elemental contents in

the pores of the sandstone sample after slurry curing, along with the presence of Na, indicating that C$_2$H$_3$NaO$_2$·3H$_2$O was generated within the sandstone. In summary, combining the results shown in Fig. 3a–f and S8, it can be concluded that when the sandstone pores are filled with slurry and cured at 35 °C, a CH$_3$COONa and SiO$_2$ mixture gradually forms. This process generates C$_2$H$_3$NaO$_2$·3H$_2$O crystals both within and on the sandstone surface.

Discussion

To investigate the sodium silicate slurry curing process in sandstone, an FBG detection system was used for temperature, humidity, and micro-strain measurements. Testing was conducted at -5 (20% RH), 15 (50% RH), 35 (40% RH), 55 (15% RH), and 75 °C (5% RH). The sandstone samples had pore diameters of 2 cm, and the experimental results are shown in Figs. 4–7.

During the sodium silicate slurry curing process at different temperatures, the slurry temperature first increased rapidly, followed by a slower increase, and reaching a peak before gradually decreasing to ambient temperature, as shown in Fig. 4a–c. This behavior can be attributed to the

Fig. 3 | Compositional and microstructural changes in the sandstone samples before and after grouting. a XRD patterns of the sandstone surface samples before and after grouting. **b** XPS full spectrum of the sandstone surface samples before and after grouting. **c–f** Si fine spectra before grouting and C, O, and Na fine spectra after grouting, respectively.
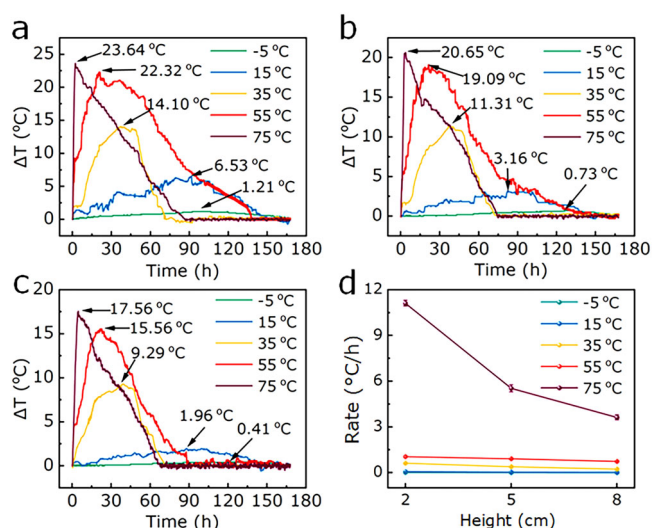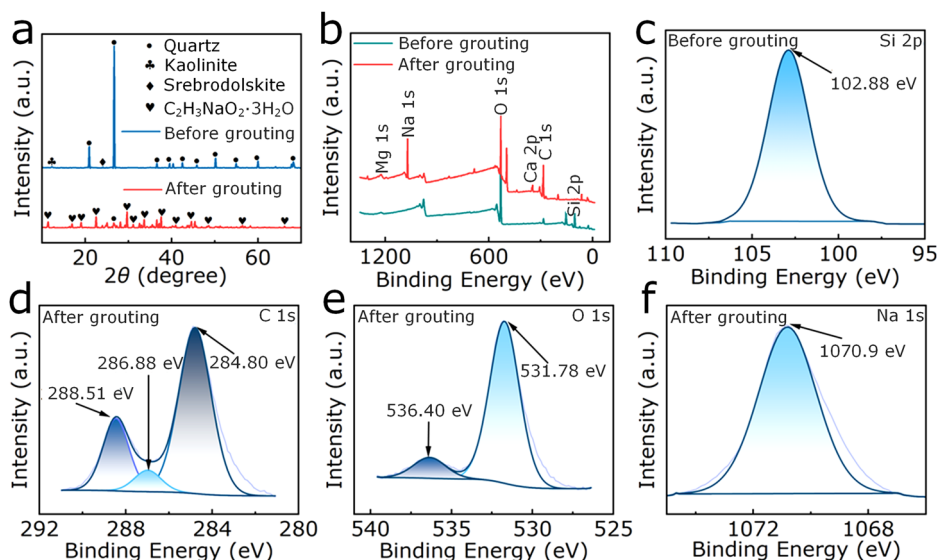
Fig. 4 | Spatial distribution of the temperature variation (ΔT) of the sodium silicate slurry within sandstone holes under different environmental temperatures during the curing process. a–c ΔT distribution within the slurry at heights of 2, 5, and 8 cm, respectively. **d** Average heating rates of the slurry at different environmental temperatures and rock heights.

following reasons: (i) $Na_2O \cdot nSiO_2$ is weakly alkaline[12,24], and reacts with CH_3COOH generated from $CH_3COOCH_2CH_2OOCCH_3$ hydrolysis, resulting in an acid-base neutralization reaction that increases the slurry local temperature. At this point, the heat released by the reaction exceeded the heat dissipated, leading to a rapid slurry temperature increase. (ii) As the curing reaction progressed, the CH_3COOH and $Na_2O \cdot nSiO_2$ concentrations within the slurry gradually decreased, resulting in a reduced amount of heat being released by the reaction. When the released heat equals the heat dissipated, the slurry temperature stabilizes. (iii) Once the curing reaction is completed, no additional heat is released and the process is dominated by heat dissipation, causing the slurry temperature to gradually decrease until it reaches the ambient temperature.

Figure 4a–c also show the internal temperature change distribution in the slurry during the sodium silicate curing at different ambient temperatures. The temperature variation magnitude comparison is as follows: 75 > 55 > 35 > 15 > -5 °C. This is because at higher ambient temperatures,

the chemical reaction intensifies, leading to a greater increase in the slurry's internal temperature. Specifically, at 75 °C, the temperature change is maximal, Reaching 23.64 °C; whereas at −5 °C, due to the extremely slow reaction within the slurry, the temperature change is negligible.

Figure 4d shows the average slurry heating rates as it increased from its initial temperature to its peak at various ambient temperatures. The results reveal a distinct heating rate distribution across different sandstone heights, specifically: 2 > 5 > 8 cm. This phenomenon can be attributed to SiO_2 accumulation at the bottom of the sandstone holes. SiO_2 has a higher density and is formed during the slurry curing process (considering that the sodium acetate density is 1.45 g/cm³, whereas the silicon dioxide density is 2.13 g/cm³). Consequently, the slurry at the bottom was cured first[36]. Furthermore, the bottom section had minimal exposure to air, and was thus the least influenced by the ambient temperature. Therefore, the reaction at 2 cm is the most vigorous, exhibiting the fastest heating rate and highest temperature, with the heating rate reaching up to 11.12 °C/h at 75 °C. By contrast, the 8-cm height experiences the greatest exposure to air, resulting in a faster heat release rate and, consequently, the slowest reaction and heating rate.

For environmental temperatures of −5 to 75 °C, the humidity of the sodium silicate slurry in the sandstone pores rapidly decreases to approximately 60% during the curing process and then gradually slows down, as shown in Fig. 5a–c. This can be attributed to the following reasons: (i) During the initial curing stage, the reaction rate between $Na_2O \cdot nSiO_2$ and CH_3COOH is fast. This leads to a rapid increase in temperature (as shown in Fig. 4), which consumes moisture inside the slurry and causes rapid evaporation, in turn resulting in a swift decrease in humidity. (ii) When the humidity decreases to approximately 60%, the slurry curing reaction is nearly complete, and the temperature decreases slowly (as shown in Fig. 4). The curing rate slows down, reducing the amount of H_2O consumed during the curing process. Consequently, moisture evaporation inside the slurry due to temperature effects also decreases, resulting in a gradual decline in humidity within the slurry, which eventually stabilizes.

Figure 5a–c also show the humidity variation distribution in the slurry during curing at different temperatures over the same curing time. The humidity variation comparison is as follows: 75 > 55 > 35 > 15 > −5 °C. This is because higher temperatures can increase the chemical reaction rate of the slurry, allowing more water to participate in the reaction within the same timeframe and moisture to evaporate more quickly at elevated temperatures[38–40]. At 15, 35, and 55 °C, a slight increase in moisture was observed at heights of 2 and 5 cm. This is because the curing process occurs sequentially from bottom to top[9]. As the slurry transitions from liquid to
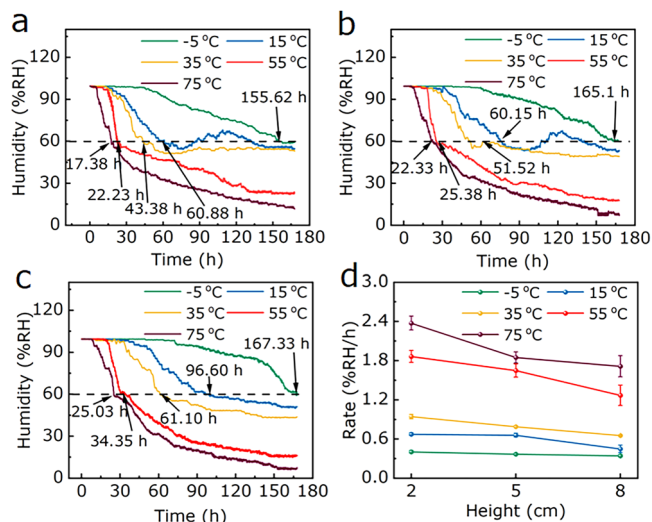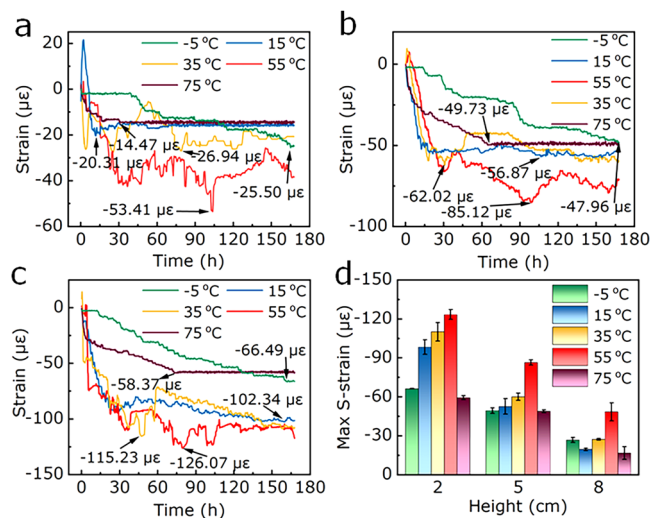
Fig. 5 | Spatial distribution of the humidity of the sodium silicate slurry within sandstone holes under different environmental temperatures during the curing process. a–c Humidity distribution within the slurry at heights of 2, 5, and 8 cm, respectively. **d** Average dehumidification rates of the slurry at different ambient temperatures and rock heights.

Fig. 6 | Spatial distribution of the micro-strain changes of the sodium silicate slurry within sandstone pores under different environmental temperatures during the curing process. a–c Strain change distribution within the slurry at heights of 2, 5, and 8 cm, respectively. **d** Maximum shrinkage strain (Max S-strain) variations of the slurry at different environmental temperatures and rock heights.

solid at heights of 2 and 5 cm, the internal porosity increases, and gravity accelerates the downward transport of pore water[41,42]. At 75 °C, the curing rate is too fast, while at −5 °C, the reaction is extremely incomplete, with the moisture reduction primarily due to H_2O freezing in the $Na_2O \cdot nSiO_2$ solution. Therefore, the "humidity increase phenomenon" does not occur at 75 or −5 °C. Additionally, Fig. 5a–c indicate that after 7 d of curing, the closer the slurry was to the top of the sandstone sample, the lower the internal humidity. At a height of 8 cm at 75 °C, the humidity reaches a minimum of 6.80%, whereas at 2 cm and −5 °C, the humidity is highest at 59.55%. This is because the slurry at the top (8 cm height) had the largest contact area with the environment, leading to the fastest moisture evaporation and the highest water molecule exchange rate with the environment. Additionally, this region had the most contact with CO_2, facilitating Reaction(3) and resulting in a rapid moisture decrease at the top of the slurry. Consequently, the humidity at a height of 8 cm remained close to the environmental relative humidity after curing.

Figure 5d shows the average dehumidification rate distribution of the slurry at different heights as it decreased from an initial humidity of approximately 100%RH to 60%RH at different temperatures. The results reveal a distinct dehumidification rate distribution across different sandstone heights, specifically: 2 > 5 > 8 cm. This is because the slurry curing occurs in a "bottom-up" manner. At a height of 2 cm, the slurry begins to react first, resulting in the earliest humidity decrease. Additionally, the slurry temperature at 2 cm was the highest (Fig. 4d), leading to the fastest reaction rate and minimal influence of external humidity, resulting in the fastest dehumidification rate. Consequently, the dehumidification rate at 2 cm height was the highest, reaching 2.38% RH/h at 75 °C.

As shown in Fig. 6a–c, at different environmental temperatures, the strain exerted by the sodium silicate slurry on the sensors during the curing process within the sandstone pores first increases, then decreases, and finally stabilizes. This can be attributed to the following reasons: (i) During the early curing stages, the rapid temperature increase (as shown in Fig. 4) leads to slight thermal expansion of the slurry, resulting in expansion strain. (ii) As curing progresses, the slurry at the top gradually transforms into CH_3COONa and SiO_2, which increases the viscosity[43,44]. Additionally, continuous moisture consumption leads to a reduction in volume, thereby increasing the shrinkage strain. (iii) When the curing of the top slurry approaches completion, the slurry converts to $C_2H_3NaO_2 \cdot 3H_2O$ and SiO_2, causing the temperature and humidity to stabilize (as shown in Figs. 4–5), resulting in a gradual internal strain stabilization within the slurry.

Figure 6a–c also show that the shrinkage strain of the slurry is highest at 55 °C. This can be attributed to the following reasons. At −5 °C, the slurry curing is extremely slow and the reaction is very incomplete, resulting in a smaller shrinkage strain. At 75 °C, the curing process occurs very rapidly. However, the excessively high temperature during curing led to significant thermal expansion strain (Fig. 2y), which counteracted some of the shrinkage strain. Additionally, rapid moisture evaporation resulted in insufficient reaction, leading to a smaller shrinkage strain at this temperature. Within a range of 15–55 °C, the slurry curing rate increases as the temperature increased. Therefore, at 55 °C, the curing rate is fast, leading to strain accumulation and an increase in strain, resulting in the most pronounced volume shrinkage during the curing process (as shown in Fig. 2i). At environmental temperatures of 15, 35, and 55 °C, a slight decrease in shrinkage strain is observed after reaching the maximum shrinkage strain. This is because the humidity increased slightly during the mid-curing stage of the slurry, leading to a mild volumetric expansion (Fig. 5a–c). Additionally, the heat generated during the curing reaction resulted in thermal expansion strain that counteracted some of the shrinkage strain, thereby reducing the overall shrinkage strain.

Figure 6d shows the maximum shrinkage strain (Max S-strain) distribution of the slurry at different heights and temperatures, which is in the order of 2 > 5 > 8 cm. This can be attributed to the fact that the slurry begins to react first at a height of 2 cm. As the slurry at the bottom underwent curing, its volume began to shrink, causing a downward displacement of the uncured slurry above it. As the reaction progresses, the slurry viscosity gradually increases[43,44]. Therefore, the slurries at heights of 5 and 8 cm experienced downward tensile strain, which counteracted a portion of their own shrinkage strain. The closer the slurry was to the top, the greater the tensile strain it experienced, leading to a larger counteraction of its own shrinkage strain. Consequently, at 55 °C, the slurry at a height of 2 cm experiences the maximum shrinkage stress, reaching up to −126.07 με.

During the sodium silicate slurry curing process, the strain on the sandstone surface at heights of 2 and 5 cm initially increases rapidly, reaches a maximum value, then gradually decreases, ultimately stabilizing, as shown Fig. 7a, b. This can be attributed to the following reasons: (i) The temperature during the curing process increases sharply, causing thermal expansion of the slurry (as shown in Figs. 2x, 2y, and 6), which exerts expansion stress on the sandstone. Additionally, the heat released during slurry curing is transferred to the sandstone body, affecting its thermal expansion and leading to an increase in micro-strain on the sandstone

surface. (ii) As the curing reaction progresses, the internal temperature of the slurry decreases (as shown in Fig. 4), resulting in a temperature decrease in both the slurry and sandstone body, which induces sandstone shrinkage, thus exhibiting a "detumescent" phenomenon[29]. As shown in Fig. 7a, b, at heights of 2 and 5 cm, the surface expansion stress exerted by the slurry on the sandstone body during curing at 75 °C is the highest, reaching 30.76 and 35.64 με, respectively. This is because at heights of 2 and 5 cm, CH_3COONa has not yet diffused to the sandstone surface to form crystalline salts (as shown in Fig. 2). Therefore, expansion strain primarily arises from thermal expansion due to the temperature increase during the sandstone curing process. The slurry experiences the highest temperature during curing at 75 °C (as shown in Fig. 4), resulting in the most significant thermal expansion and maximum expansion strain.

Figure 7c shows that at a height of 8 cm in the sandstone sample, when the environmental temperature during slurry curing is 15 °C, the surface strain exerted by the curing slurry on the sandstone sample continues to increase. After the curing time exceeds 100 h, the surface stress on the sandstone body rapidly increases, reaching a micro-stress change of 55.02 με at a curing time of 165 h. This can be attributed to the following reasons: (i) At 15 °C, CH3COONa migration from the inside at a height of 8 cm is the greatest (as shown in Fig. 2b, i), resulting in the maximum expansion strain on the sandstone body. (ii) The temperature increase during the curing process exerts thermal expansion on the sandstone. Additionally, the elevated temperature further promotes rapid CH_3COONa diffusion from the inside of the sandstone outward, leading to the formation of

$C_2H_3NaO_2 \cdot 3H_2O$ crystals and an increase in the expansion strain. Additionally, Fig. 7c shows that when the slurry curing temperatures are 35, 55, and 75 °C, the surface stress exerted on the sandstone body exhibits a "detumescent" phenomenon[29]. This can be attributed to the thermal expansion effects generated during slurry curing. At a height of 8 cm, the strain in sandstone at 35–75 °C is primarily due to thermal expansion of both grout and sandstone matrix, decreasing with grout temperature drop. However, at 15 °C, the strain mainly results from inward-to-outward migration during grout curing, forming $C_2H_3NaO_2 \cdot 3H_2O$ crystals on the surface, leading to continuous surface strain increase. Since temperature has a minor impact on strain, the "detumescent" phenomenon does not occur.

Figure 7d shows the maximum expansion strain distribution exerted by the slurry on the sandstone body during curing at different temperatures at various heights on the sandstone sample, which is in the order of 8 > 5 > 2 cm. This is because the closer the slurry is to the sandstone holes, the greater the slurry migration to the sandstone surface (as shown in Fig. 2), resulting in a maximum expansion strain at 8 cm which reaches to 55.02 με.

Based on Figs. 2 to 7, the curing mechanism of sodium silicate slurry can be summarized as follows: Initially, $CH_3COOCH_2CH_2OOCCH_3$ in the sodium silicate slurry undergoes hydrolysis to produce CH_3COOH, which reacts with $Na_2O \cdot nSiO_2$, resulting in an increase in temperature, a decrease in humidity and strain, and the formation of SiO_2 solid and CH_3COONa. Subsequently, the heat, CH_3COONa, and moisture in the slurry are transported along the pores of the sandstone to the surface, causing expansion strain. Finally, as the moisture evaporates, the CH_3COONa solution gradually transforms into $C_2H_3NaO_2 \cdot 3H_2O$ crystals, which adhere to the surface of the sandstone. The mechanism diagram is shown in Fig. 8.

Additionally, it can be observed that at 75 °C, the reaction of the slurry in the 2 cm-diameter holes is the most vigorous, resulting in the largest temperature and humidity changes, as well as the fastest change rates. This leads to incomplete reactions and significant structural damage to the curing products. At 55 °C, the rapid curing rate causes excessive internal shrinkage strain, resulting in noticeable volume contraction, the formation of numerous acicular crystals, and crack development, which diminishes the restoration effectiveness. At 15 °C, the slower curing rate and greater CH_3COONa migration result in the maximum surface strain on the sandstone, causing severe damage to the surface morphology of artifacts. At −5 °C, the internal reactions of the slurry are highly incomplete and slow, leading to structural instability. By contrast, at 35 °C, the curing rate is moderate, allowing for the most thorough internal reactions, with an average heating rate of 0.42 °C/h, an average moisture loss rate of 0.79% RH/h, and a maximum shrinkage strain of −115.23 με. Some reaction products diffused into the sandstone body, forming $C_2H_3NaO_2 \cdot 3H_2O$, which enhanced the bonding strength between the slurry and sandstone. Consequently, the maximum micro-strain exerted on the sandstone body was 31.62 με, resulting in minimal damage. Therefore, when using sodium silicate slurry for grouting restorations in rock cave cracks, a temperature of approximately 35 °C yields the best results.

To study the sodium silicate grout curing process inside sandstone at a temperature of 35 °C and relative humidity of 40%, the grout temperature, humidity, and micro-strain changes within samples with crack holes of
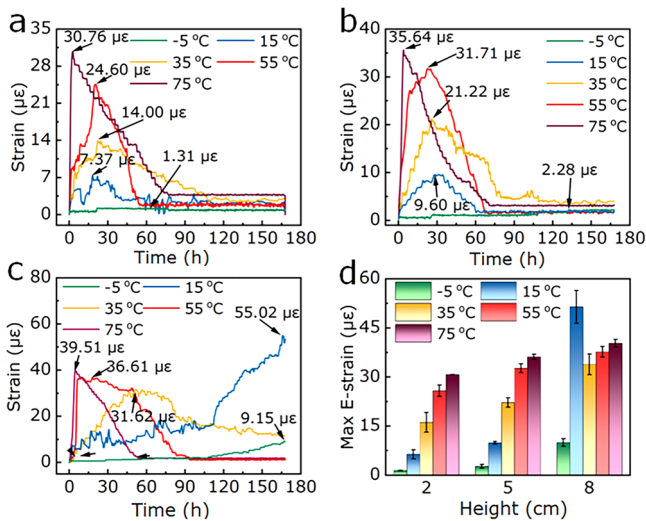
Fig. 7 | Spatial distribution of micro-strain on the sandstone surface during the sodium silicate slurry curing process at different environmental temperatures. a–c Strain change distribution within the sandstone surface at heights of 2, 5, and 8 cm, respectively. **d** Maximum expansion strain (Max E-Strain) variations on the sandstone surface under different environmental temperatures and rock heights.

Fig. 8 | Mechanism diagram of sodium silicate slurry curing process.
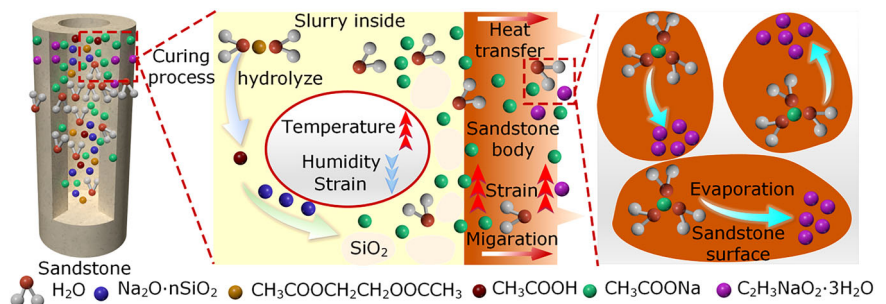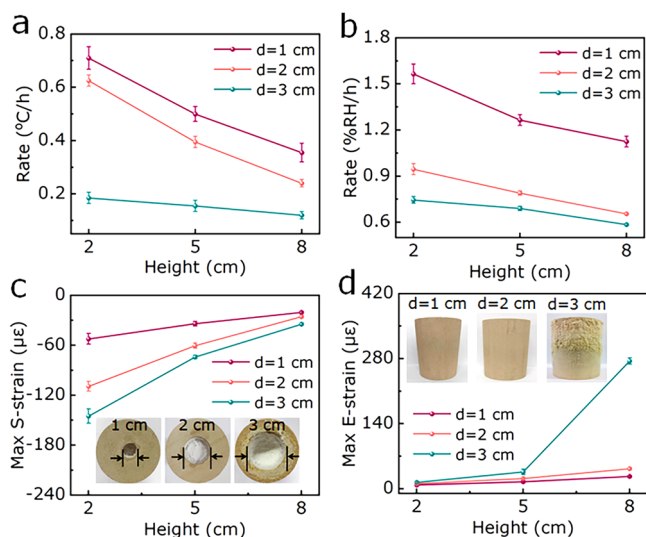
Fig. 9 | Distribution information of parameters during the curing process of sodium silicate slurry inside sandstones with different pore sizes. a–c Average grout heating rate, dehumidification rate, and maximum micro-strain, respectively. **d** Maximum micro-strain on the sandstone surface during the sodium silicate slurry curing process inside sandstone with holes of different diameters at 35 °C. The insets in (**c**, **d**) show images of the top and side surfaces of the grout after curing inside the sandstone pores.

different diameters (1–3 cm) were monitored. Additionally, the micro-strain spatial distribution on the sandstone surface was examined. The experimental results are shown in Fig. 9 and Figs. S10–S14.

Figure 9a shows the ranking of the average slurry heating rates in sandstone with holes of different diameters when the temperature reached its maximum; the raking is as follows: 1 > 2 > 3 cm. This is attributed to the fact that smaller holes reduce the heat dissipation area, making the slurry temperature less affected by the ambient temperature and thus heating up faster. Therefore, the slurry cured at the highest temperature (Fig. S10a) in the 1 cm-diameter hole, with the fastest reaction and heating rates, reaching 0.71 °C/h. By contrast, in the 3-cm-diameter hole, the slurry had the largest contact area with air and the largest heat-dissipation area, leading to the fastest heat release rate. This resulted in the slowest reaction rate, least temperature increase (Fig. S10c), and slowest heating rate (0.12 °C/h).

Figure 9b shows the ranking of the average slurry dehumidification rates in sandstone with holes of different diameters as the humidity decreased from approximately 100% to 60% during the curing process; the ranking is as follows: 1 > 2 > 3 cm (Fig. S11). This is because as the sandstone hole diameter decreased, the slurry volume decreased, resulting in a faster curing reaction rate. This led to a higher internal temperature of the slurry (Fig. S10a) and a higher moisture consumption and evaporation rate. Consequently, slurry curing in the 1-cm-diameter hole exhibits the fastest dehumidification rate, reaching 1.57% RH/h.

Figure 9c shows the ranking of the maximum shrinkage strains (Max S-strain) of the slurry in sandstone with holes of different diameters; the ranking is as follows: 3 > 2 > 1 cm (Fig. S12). This is because, as the sandstone hole diameter increased, the slurry volume increased, resulting in more slurry participating in the reaction. This led to a greater shrinkage volume and shrinkage micro-strain during the measurement (see the inset in Fig. 9c). Consequently, the slurry in the 3 cm-diameter hole exhibits the largest shrinkage strain, reaching -151.11 µε. Conversely, in smaller sandstone cracks, less slurry participates in the reaction, resulting in a smaller shrinkage volume and micro-strain; therefore, the slurry in the 1-cm-diameter hole exhibits the smallest shrinkage strain (-19.53 µε).

Figure 9d shows the ranking of the maximum expansion micro-strain (Max E-strain) generated on the sandstone surface during slurry curing in holes of different sizes; the ranking is as follows: 3 > 2 > 1 cm (Fig. S13). This

is because, as the sandstone hole diameter increases, the sandstone becomes thinner and smaller, facilitating the transfer of heat, H_2O, and CH3COONa to the sandstone surface (Fig. S14 and inset in Fig. 9d). As a result, the surface expansion strain of the sample with a 3-cm-diameter hole was larger, reaching 279.71 µε. Conversely, in smaller sandstone cracks, the volume of the stone is larger, making deformation more difficult, and the crystallization area on the sandstone surface is smaller, resulting in a lower expansion strain. Therefore, the sample with a 1-cm-diameter hole had the smallest crystallization area (Fig. S14 and inset in Fig. 9d) and a minimum micro-strain of 6.44 µε. Overall, from Figs. 9 and S10–S14, it can be concluded that the sodium silicate slurry is more suitable for repairing smaller cracks in rock caves.

In this paper, a new method for in situ continuous decoding of temperature, humidity, and micro-strain in the process of repairing sandstone cracks with sodium silicate slurry is proposed using an FBG array system. A theoretical model was established to measure the temperature, humidity, and micro-strain. In situ and continuous decoding provided spatial distribution information on the temperature, humidity, micro-strain of the slurry and the micro-strain of the sandstone surface under different environmental temperatures and hole diameters. Offline techniques such as optical microscopy, field-emission scanning electron microscopy, X-ray diffraction, and X-ray photoelectron spectroscopy were employed to analyze the surface morphological and material compositional changes.

The experimental results showed that within an environmental temperature range of −5 to 75 °C, when the environmental temperature was 35 °C, the curing reaction was completed, resulting in the densest cured slurry structure. Additionally, during the curing reaction, the curing product CH_3COONa was partially transferred to the interior of the sandstone to form $C_2H_3NaO_2 \cdot 3H_2O$ crystals. This process enhanced the bonding strength between the slurry and sandstone, generating a small expansion strain of 31.62 µε on the sandstone body, while causing slight influence to the cultural relics. Additionally, during the grouting restoration of sandstone with different hole diameters at an environmental temperature of 35 °C, both the slurry micro-strain and the surface strain induced on the sandstone body increased with crack diameter. Therefore, the sodium silicate slurry is more suitable for repairing small cracks in sandstone at an environmental temperature of 35 °C.

The findings of this study revealed the curing mechanisms of grouting materials in sandstone holes and the interaction between the slurry and sandstone. Additionally, they highlight the extent of damage caused by slurry to cultural relics and the effectiveness of hole restoration in rock caves. The methodology and findings of this study contribute to advancements in the protection of cultural heritage and promotes the development of optical fiber sensors and their detection technologies. This enhances the intelligent technological protection of cultural relics, thereby holding significant scientific research significance and engineering application value.

Data availability
No datasets were generated or analysed during the current study.

References
1. Wang, G. et al. Sandstone protection by using nanocomposite coating of silica. *Appl Surf. Sci.* **615**, 156193, https://doi.org/10.1016/j.apsusc.2022.156193 (2023).
2. Wang, X., Wang, Y., Guo, Q., Pei, Q. & Zhao, G. The history of rescuing reinforcement and the preliminary study of preventive protection system for the cliff of Mogao Grottoes in Dunhuang, China. *Herit. Sci.* **9**, 58, https://doi.org/10.1186/s40494-021-00537-w (2021).
3. Hao, Y., Yao, Z., Wu, R. & Bao, Y. Damage and restoration technology of historic buildings of brick and wood structures: a review. *Herit. Sci.* **12**, 301, https://doi.org/10.1186/s40494-024-01422-y (2024).

4. Shu, X. et al. Anchorage mechanism and parametric analysis of a novel interface-shear-stress-dispersing bolt. *unn. Undergr. Sp. Tech.* **154**, 106118, https://doi.org/10.1016/j.tust.2024.106118 (2024).

5. Maravelaki-Kalaitzaki, P., Bakolas, A., Karatasios, I. & Kilikoglou, V. Hydraulic lime mortars for the restoration of historic masonry in Crete. *Cem. Concr. Res* **35**, 1577–1586, https://doi.org/10.1016/j.cemconres.2004.09.001 (2005).

6. da Rocha Gomes, S., Ferrara, L., Sánchez, L. & Moreno, M. S. A comprehensive review of cementitious grouts: Composition, properties, requirements and advanced performance. *Constr. Build Mater.* **375**, 130991, https://doi.org/10.1016/j.conbuildmat.2023.130991 (2023).

7. Sepulcre-Aguilar, A. & Hernández-Olivares, F. Assessment of phase formation in lime-based mortars with added metakaolin, Portland cement and sepiolite, for grouting of historic masonry. *Cem. Concr. Res.* **40**, 66–76, https://doi.org/10.1016/j.cemconres.2009.08.028 (2010).

8. Zhou, Y. et al. Experimental investigation of strength repairing effects of chemical grouting on fractured porous sandstone under different temperature conditions. *Int J. Rock. Mech. Min.* **170**, 105552, https://doi.org/10.1016/j.ijrmms.2023.105552 (2023).

9. Matinfar, M. & Nychka, J. A. A review of sodium silicate solutions: Structure, gelation, and syneresis. *Adv Colloid Interfac.* 103036. https://doi.org/10.1016/j.cis.2023.103036 (2023).

10. Fang, S., Zhang, K., Zhang, B. & Wang, L. Evaluation of cement-based grout for reinforcing unsafe rocks of stone carvings at Hangzhou Klippe in China. *J. Mater. Civ. Eng.* **31**, 05018005 (2019).

11. Peng, G. et al. Research on workability, mechanics, and durability of cementitious grout: A critical review. *Constr. Build Mater.* **449**, 138374, https://doi.org/10.1016/j.conbuildmat.2024.138374 (2024).

12. Gualtieri, M. L., Romagnoli, M., Pollastri, S. & Gualtieri, A. F. Inorganic polymers from laterite using activation with phosphoric acid and alkaline sodium silicate solution: Mechanical and microstructural properties. *Cem. Concr. Res* **67**, 259–270, https://doi.org/10.1016/j.cemconres.2014.08.010 (2015).

13. Yoo, D.-Y., Ryu, G.-S., Yuan, T. & Koh, K.-T. Mitigating shrinkage cracking in posttensioning grout using shrinkage-reducing admixture. *Cem. Concr. Comp.* **81**, 97–108, https://doi.org/10.1016/j.cemconcomp.2017.05.005 (2017).

14. Wu, H. et al. In-situ monitoring of changes in temperature and microstrain during the chemical corrosion of stone cultural relics. *Herit. Sci.* **12**, 345, https://doi.org/10.1186/s40494-024-01439-3 (2024).

15. Liu, K., Liu, B., Ostadhassan, M. & Safaei-Farouji, M. Quantifying Microstrain of Quartz and Illite During Thermal Maturation of Organic Matter. *Rock. Mech. Rock. Eng.* **56**, 9189–9199, https://doi.org/10.1007/s00603-023-03452-7 (2023).

16. Hu, X., Yang, B., Peng, G., Zhong, S. & Zhang, H. Investigation on hydration behavior and microscopic pore structure of early-age cement-based grouting material. *J. Build Eng.* **80**, 108050, https://doi.org/10.1016/j.jobe.2023.108050 (2023).

17. Liu, W., Liang, J. & Xu, T. Tunnelling-induced ground deformation subjected to the behavior of tail grouting materials. *Tunn. Undergr. Sp. Tech.* **140**, 105253, https://doi.org/10.1016/j.tust.2023.105253 (2023).

18. Yang, Z. et al. Flexible and stretchable polyurethane/waterglass grouting material. *Constr. Build Mater.* **138**, 240–246, https://doi.org/10.1016/j.conbuildmat.2017.01.113 (2017).

19. Liu, W., Sun, Y., Meng, X. & Qin, Y. Experimental analysis of Nano-SiO_2 modified waterborne epoxy resin on the properties and microstructure of cement-based grouting materials. *Energy* **268**, 126669, https://doi.org/10.1016/j.energy.2023.126669 (2023).

20. Li, S. et al. Investigation of the applicability of infrared thermography detection of grouting voids in prestressed tendon ducts under hydration heat excitation. *Ndte Int* **143**, 103055, https://doi.org/10.1016/j.ndteint.2024.103055 (2024).

21. Singh, M. J. et al. Applications of fibre Bragg grating sensors for monitoring geotechnical structures: A comprehensive review. *Measurement* **218**, 113171, https://doi.org/10.1016/j.measurement.2023.113171 (2023).

22. Palumbo, G. et al. Fiber Bragg grating sensors for real time monitoring of early age curing and shrinkage of different metakaolin-based inorganic binders. *IEEE Sens J.* **19**, 6173–6180, https://doi.org/10.1109/JSEN.2019.2908728 (2019).

23. Guo, J.-Y. et al. Application of PI-FBG sensor for humidity measurement in unsaturated soils. *Measurement* **188**, 110415, https://doi.org/10.1016/j.measurement.2021.110415 (2022).

24. Zhou, Y. et al. Experimental investigation on the grouting diffusion characteristics and relative filling degree of chemical slurry in fractured porous sandstone. *Rock. Mech. Rock. Eng.* **56**, 7819–7837 (2023).

25. Wang, Y., Yu, K., Peng, H. & Ling, X. Preparation and thermal properties of sodium acetate trihydrate as a novel phase change material for energy storage. *Energy* **167**, 269–274, https://doi.org/10.1016/j.energy.2018.10.164 (2019).

26. Xu, Y., Zhang, Y., Huang, J. & Chen, G. Mechanical properties, microstructure and consolidation of sand modified with sodium silicate. *Eng. Geol.* **310**, 106875, https://doi.org/10.1016/j.enggeo.2022.106875 (2022).

27. Borisova, D., Möhwald, H. & Shchukin, D. G. Mesoporous silica nanoparticles for active corrosion protection. *Acs Nano* **5**, 1939–1946, https://doi.org/10.1021/nn102871v (2011).

28. Zhong, N., Chen, M., Wang, Z., Xin, X. & Li, B. Photochemical device for selective detection of phenol in aqueous solutions. *Lab Chip* **18**, 1621–1632, https://doi.org/10.1039/C8LC00317C (2018).

29. Xu, C. et al. In situ detection of spatial distribution information of temperature-pH-strain of sandstone cultural relics. *Npj Mat. Degrad.* **8**, 31, https://doi.org/10.1038/s41529-024-00438-w (2024).

30. Fan, A. et al. Cementation and porosity evolution of tight sandstone reservoirs in the Permian Sulige gas field, Ordos Basin (central China). *Mar. Pet. Geol.* **103**, 276–293, https://doi.org/10.1016/j.marpetgeo.2019.02.010 (2019).

31. Dill, H. G. Kaolin: Soil, rock and ore. *Miner. Magmat., Sediment. metamorphic Environ. Earth-Sci. Rev.* **161**, 16–129, https://doi.org/10.1016/j.earscirev.2016.07.003 (2016).

32. Wang, X. et al. Effects of metakaolin on sulfate and sulfuric acid resistance of grouting restoration materials. *Constr. Build Mater.* **349**, 128714, https://doi.org/10.1016/j.conbuildmat.2022.128714 (2022).

33. Kang, S.-H., Hong, S.-G. & Moon, J. Shrinkage characteristics of heat-treated ultra-high performance concrete and its mitigation using superabsorbent polymer based internal curing method. *Cem. Concr. Comp.* **89**, 130–138, https://doi.org/10.1016/j.cemconcomp.2018.03.003 (2018).

34. Qin, G. et al. Nitrogen-rich carbon/SiO2 nanotubes composites prepared by self-assembly as high-performance anode lithium-ion battery. *Int J. Hydrog. Energ.* **49**, 39–50, https://doi.org/10.1016/j.ijhydene.2023.09.201 (2024).

35. Dorey, S., Gaston, F., Marque, S. R. A., Bortolotti, B. & Dupuy, N. XPS analysis of PE and EVA samples irradiated at different γ-doses. *Appl Surf. Sci.* **427**, 966–972, https://doi.org/10.1016/j.apsusc.2017.09.001 (2017).

36. Al-Gaashani, R., Najjar, A., Zakaria, Y., Mansour, S. & Atieh, M. XPS and structural studies of high quality graphene oxide and reduced graphene oxide prepared by different chemical oxidation methods. *Ceram. Int* **45**, 14439–14448, https://doi.org/10.1007/s00603-020-02063-w (2019).

37. Zhou, J.-H. et al. Characterization of surface oxygen complexes on carbon nanofibers by TPD, XPS and FT-IR. *Carbon* **45**, 785–796, https://doi.org/10.1016/j.carbon.2006.11.019 (2007).

38. Gao, C. W., Allen, J. W., Green, W. H. & West, R. H. Reaction Mechanism Generator: Automatic construction of chemical kinetic

mechanisms. *Comput Phys. Commun.* **203**, 212–225, https://doi.org/10.1016/j.cpc.2016.02.013 (2016).

39. Wang, W. et al. Global lake evaporation accelerated by changes in surface energy allocation in a warmer climate. *Nat. Geosci.* **11**, 410–414, https://doi.org/10.1038/s41561-018-0114-8 (2018).

40. Chang, E.-E., Chen, C.-H., Chen, Y.-H., Pan, S.-Y. & Chiang, P.-C. Performance evaluation for carbonation of steel-making slags in a slurry reactor. *J. Hazard Mater.* **186**, 558–564, https://doi.org/10.1016/j.jhazmat.2010.11.038 (2011).

41. Kermani, M., Hassani, F., Aflaki, E., Benzaazoua, M. & Nokken, M. Evaluation of the effect of sodium silicate addition to mine backfill, Gelfill− Part 1. *J. Rock. Mech. Geotech.* **7**, 266–272, https://doi.org/10.1016/j.jrmge.2015.03.006 (2015).

42. Yuan, H., Zhang, Z., Huang, X. & Li, Y. Comparing, slurry infiltration characteristics between calcareous and silica sands based on slurry infiltration column tests and CT scanning. *Tunn. Undergr. Sp. Tech.* **152**, 105919, https://doi.org/10.1016/j.tust.2024.105919 (2024).

43. Zhu, Z. et al. Study of the viscosity-temperature characteristics of cement-sodium silicate grout considering the time-varying behaviour of viscosity. *Constr. Build Mater.* **306**, 124818, https://doi.org/10.1016/j.tust.2024.105919 (2021).

44. Wang, W., Zhao, W., Zhang, J. & Zhou, J. Epoxy-based grouting materials with super-low viscosities and improved toughness. *Constr. Build Mater.* **267**, 121104, https://doi.org/10.1016/j.conbuildmat.2020.121104 (2021).

Acknowledgements

Author contributions

N.Z. designed an experimental protocol. R.Z. Conducted the experiments. Under the support of Y.H. and N.Z., Y.L. and Q.X. conducted the calibration and encapsulation of the sensors, and performed the characterization of sandstone and slurry; R.Z. and N.Z. recorded, analyzed, and interpreted the data. R.Z. and N.Z. completed the drafting of the manuscript. R.Z., Y.H., Q.X., Y.L., and N.Z. revised the manuscript. N.Z., Y.H., Q.X., and Y.L. offered the Funding acquisition. All authors have read and approved the final manuscript.

Competing interests

The authors declare no competing interests.

Additional information

Publisher's note Springer Nature remains neutral with regard to jurisdictional claims in published maps and institutional affiliations.